

Impedance Analysis of Modular Multi-Level Converters Connected to Weak AC Grids

Javad Khazaei ¹, *Member, IEEE*, Mebtu Beza ², *Member, IEEE*, and Massimo Bongiorno, *Senior Member, IEEE*

Abstract—This paper investigates the stability of a modular multi-level converter (MMC) based HVDC system connected to a weak ac grid. Impedance analysis is used to study the interactions between the weak ac grid and the converter. For this, the impedance of the MMC is first derived considering various outer- and inner-loop controllers. The Nyquist-stability criterion is then used to analyze the stability of the MMC connected to the weak ac grid for various case studies. The impact of circulating current controller on the stability of the MMC connected to the weak ac grid is also validated for two different types of outer-loop controllers. Finally, time-domain simulations are carried out using MATLAB/Simscap Power System toolbox to validate the analytical results.

Index Terms—Modular multi-level converter (MMC), weak ac Grid, proportional resonant control, short circuit ratio (SCR).

I. INTRODUCTION

MODULAR multi-level converter (MMC) is the preferred choice now for voltage source converter (VSC)-based HVDC systems in high power applications because of its low power loss, high scalability, and low harmonics content [1]–[4].

So far, researchers have focused on modeling, control, and design of MMC-based HVDC systems, especially for circulating current mitigation, or submodule (SM)-capacitor voltage-unbalance compensation [5]–[7]. However, there has not been much attention to stability analysis or control limitations of the MMC-based HVDC systems. Among the few existing literature, [8] developed a steady-state model for an MMC to describe the explicit analytical relationship for various voltage and current quantities. The state-space approach was used in [9] to model the dominant modes of the MMC with different controllers and capability curves were used to analyze the system under different conditions. The impact of three different MMC topologies under dc-fault conditions was studied in [10]. A frequency-domain stability analysis of MMC-based HVDC system for wind farm integration was studied recently in [11].

It was shown recently that a two-level VSC enhanced with a vector control experiences stability issues while connected to

a weak ac grid [12]–[15]. The stability analysis of a two-level VSC connected to a weak ac grid has been widely studied in the literature. Several studies have introduced new alternatives for interconnection of a VSC to a weak ac grid such as: advanced vector control [12], robust vector control [13], and power synchronization control [14]. However, stability and interactions of an MMC system connected to a weak ac grid has not yet been addressed. Although two-level VSCs and MMCs share similar characteristics, the complicated dynamics and the extra controllers of MMCs may impact the system's performance in weak ac-grid connections.

The main contribution of this paper is to analyze the performance of the MMC system when connected to a weak ac grid. Impedance analysis is a useful technique to investigate dynamic interactions between converters and grids [16]–[20]. The main concept of the impedance analysis was firstly introduced in [16] for grid-connected VSCs. Reference [17] discussed the synchronization issue of VSCs controlled in dq -frame. It was shown that the negative incremental resistance behavior of grid-connected VSCs was due to the phase-locked loop (PLL) control and changing the PLL design could improve the synchronization procedure. As another example, sub-synchronous oscillations and resonances between an HVDC rectifiers and a wind farm was studied in [18] using the impedance models. Interactions between wind farm controllers and HVDC rectifier were studied by frequency responses of the converter impedance. It was concluded that if the bandwidth of a wind farm controller was faster than the bandwidth of an HVDC rectifier, resonances would occur. The authors have extensively studied the resonances between the two-level VSCs and the grid using both dc and ac impedance modeling in [19] and [20]. The impact of power-transfer levels and dc-voltage controller on the resonances between the HVDC converter and the grid was analyzed using the impedance models. However, the impedance model of an MMC is different from a two-level VSC in [11] and [21]. The impedance of an MMC connected to an offshore wind farm was derived in [11] and a frequency analysis was carried out to investigate the effect of circulating current controller on the stability of the combined system. Furthermore, the dc impedance of an MMC system was derived in [21] and the effect of circulating current controller on the dc impedance was addressed. However, the derived impedance models in the aforementioned works did not consider the impact of outer-loop controllers, the PLL, and the inner-current controller. In addition, the strength of the system was not considered in the analysis which can significantly affect the interactions between the converter and the grid. Therefore, this paper proposes the impedance derivation of an MMC including the internal dynamics of the MMC, the

Manuscript received April 7, 2017; revised July 30, 2017 and October 23, 2017; accepted November 26, 2017. Date of publication December 4, 2017; date of current version June 18, 2018. Paper no. TPWRS-00505-2017. (Corresponding author: Javad Khazaei.)

J. Khazaei is with the School of Science, Engineering and Technology, Penn State Harrisburg, Middletown, PA 17057 USA (e-mail: jxk792@psu.edu).

M. Beza and M. Bongiorno are with the Department of Electrical Engineering, Division of Electric Power Engineering, Chalmers University of Technology, Gothenburg 412 96, Sweden (e-mail: mebtu.beza@chalmers.se; massimo.bongiorno@chalmers.se).

Color versions of one or more of the figures in this paper are available online at <http://ieeexplore.ieee.org>.

Digital Object Identifier 10.1109/TPWRS.2017.2779403

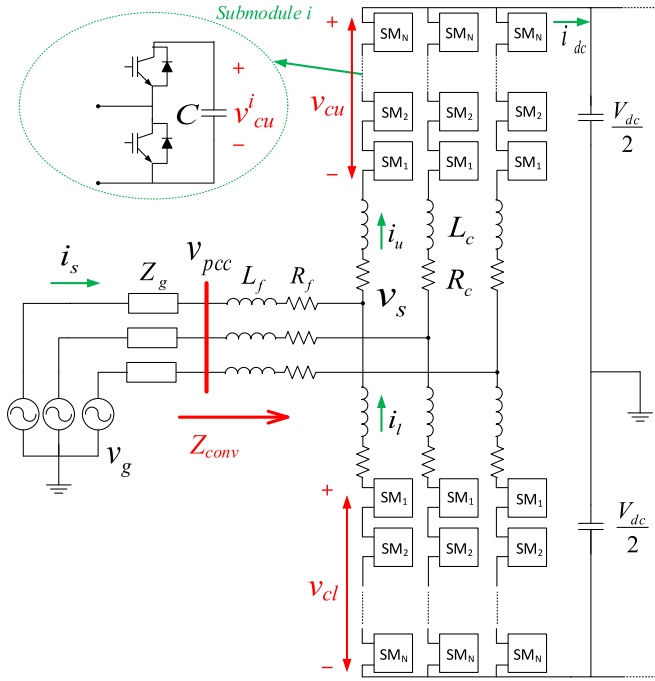


Fig. 1. Basic diagram of a modular multi-level converter connected to the grid.

circulating-current controller, the inner-current controller, the outer-loop controllers, and the PLL. Unlike the existing literature, the impact of a weak ac grid on the stability of the MMC system with various control structures and/or parameters is also explored. The Nyquist-stability criterion is used to analyze the resonances and interactions between the MMC and the grid for multiple scenarios. Finally, time-domain simulations are performed to verify the analytical results in various case studies.

The rest of the paper is as follows: Section II describes the ac impedance derivation for an MMC and Section III addresses the stability analysis of the MMC connected to a weak grid using the impedance models in Section II. Various case studies are carried out in Section IV and the paper concludes in Section V.

II. AC IMPEDANCE DERIVATION

The ac impedance of the converter ($Z_{conv}(s)$) is derived as $Z_{conv}(s) = \frac{\Delta v_{pcc}(s)}{\Delta i_s(s)}$, where v_{pcc} is the voltage at the point of common coupling (PCC) and i_s is the current flowing from the grid to the converter. For this purpose, a relationship between Δv_{pcc} and Δi_s should be developed in the dq reference frame. Considering Fig. 1, the lower and the upper arms are symmetric and the corresponding currents in each arm can be expressed as:

$$\begin{aligned} i_u^k &= \frac{i_s^k}{2} + i_c^k \\ i_l^k &= \frac{-i_s^k}{2} + i_c^k \end{aligned} \quad (1)$$

where i_c^k represents the circulating current. In the notations, a superscript k represents different phases of the converter ($k = a, b, c$), and subscripts u and l refer to the upper and the lower arms, respectively. Using the Kirchhoff's voltage law (KVL)

for the upper and the lower arms in each phase in Fig. 1, we have [22]:

$$v_{pcc}^k = L_f \frac{di_s^k}{dt} + R_f i_s^k + L_c \frac{di_u^k}{dt} + R_c i_u^k - v_{cu}^k + \frac{V_{dc}}{2} \quad (2)$$

$$v_{pcc}^k = L_f \frac{di_s^k}{dt} + R_f i_s^k - L_c \frac{di_l^k}{dt} - R_c i_l^k + v_{cl}^k - \frac{V_{dc}}{2} \quad (3)$$

Using (1)–(3), the ac-side current (i_s^k) and the circulating current (i_c^k) dynamics of the system can be expressed as [23]:

$$v_{pcc}^k = L_t \frac{di_s^k}{dt} + R_t i_s^k + \frac{1}{2} (v_{cl}^k - v_{cu}^k) \quad (4)$$

$$0 = L_c \frac{di_c^k}{dt} + R_c i_c^k - \frac{1}{2} (v_{cl}^k + v_{cu}^k) + \frac{V_{dc}}{2} \quad (5)$$

where $L_t = L_f + \frac{L_c}{2}$, $R_t = R_f + \frac{R_c}{2}$, and v_{cl}^k and v_{cu}^k represent the total inserted voltages in the lower and the upper arms. Using the total submodule voltages in the lower and the upper arms ($v_{cl}^{\sum k}$ and $v_{cu}^{\sum k}$), the inserted voltages (v_{cl}^k and v_{cu}^k) can be expressed as [23]:

$$\begin{aligned} v_{cl}^k &= n_l^k v_{cl}^{\sum k}, \quad n_l^k = \frac{\frac{V_{dc}}{2} + v_s^{*k} - v_c^{*k}}{V_{dc}} \\ v_{cu}^k &= n_u^k v_{cu}^{\sum k}, \quad n_u^k = \frac{\frac{V_{dc}}{2} - v_s^{*k} - v_c^{*k}}{V_{dc}} \end{aligned} \quad (6)$$

where, V_{dc} is the converter dc voltage, v_s^{*k} and v_c^{*k} are the internal converter voltage references that derive the currents i_s^k and i_c^k , respectively. By substituting (6) in (4) and (5), the small-signal dynamic model of the system can be expressed:

$$\Delta v_{pcc}^k = L_t \frac{d\Delta i_s^k}{dt} + R_t \Delta i_s^k + C_1 \Delta v_{cl}^{\sum k} + C_2 \Delta v_{cu}^{\sum k} + \Delta v_s^{*k} \quad (7)$$

$$0 = L_c \frac{d\Delta i_c^k}{dt} + R_c \Delta i_c^k - C_1 \Delta v_{cl}^{\sum k} + C_2 \Delta v_{cu}^{\sum k} + \Delta v_c^{*k} \quad (8)$$

where $C_1 = \frac{1}{4} + \frac{v_{s0}^{*k}}{2V_{dc}}$ and $C_2 = -\frac{1}{4} + \frac{v_{s0}^{*k}}{2V_{dc}}$. The notation Δx represents a small perturbation around a steady-state operating point x_0 . For the steady-state values, it is considered that $v_{c0}^{*k} \ll V_{dc}$ and $v_{cl0}^{\sum k} = v_{cu0}^{\sum k} = V_{dc}$. These assumptions are acceptable as the steady-state ripples in $v_{cl0}^{\sum k}$ and $v_{cu0}^{\sum k}$ are much smaller than the steady-state dc-link voltage, V_{dc} . Moreover, the impact of the dc-link voltage on the ac-side input admittance is small and therefore assumed constant only for the purpose of the ac-side input impedance derivation [24].

The next step in the input impedance derivation is to express $v_{cl}^{\sum k}$ and $v_{cu}^{\sum k}$ in (7) in terms of v_{pcc}^k , i_s^k and v_s^{*k} . Assuming the individual submodule capacitor voltages are equal and using the fact that the instantaneous power in an arm of the MMC represents the rate of change of stored energy in the total capacitors in the same arm, the dynamics in $v_{cl}^{\sum k}$ and $v_{cu}^{\sum k}$ can be expressed as [23]:

$$\frac{C}{N} \frac{dv_{cu,l}^{\sum k}}{dt} = -n_{u,l}^k i_{u,l}^k \quad (9)$$

where C is the capacitance of the submodule (SM), N is the total number of submodules, and $n_{u,l}^k$ is derived based on (6).

By substituting (6) into (9), and using (1), the dynamics in (9) can be rewritten as:

$$\begin{aligned} \frac{C}{N} \frac{dv_{cl}^{\sum k}}{dt} &= \left(\frac{1}{4} + \frac{v_s^{*k} - v_c^{*k}}{2V_{dc}} \right) i_s^k - \left(\frac{1}{2} + \frac{v_s^{*k} - v_c^{*k}}{V_{dc}} \right) i_c^k \\ \frac{C}{N} \frac{dv_{cu}^{\sum k}}{dt} &= \left(\frac{-1}{4} + \frac{v_s^{*k} + v_c^{*k}}{2V_{dc}} \right) i_s^k + \left(\frac{-1}{2} + \frac{v_s^{*k} + v_c^{*k}}{V_{dc}} \right) i_c^k \end{aligned} \quad (10)$$

Applying the small-signal analysis to (10), we have:

$$\begin{aligned} \frac{C}{N} \frac{dv_{cl}^{\sum k}}{dt} &= C_1 \Delta i_s^k + C_3 \Delta v_s^{*k} + 2C_1 \Delta i_c^k - C_3 \Delta v_c^{*k} \\ \frac{C}{N} \frac{dv_{cu}^{\sum k}}{dt} &= C_2 \Delta i_s^k + C_4 \Delta v_s^{*k} + 2C_2 \Delta i_c^k + C_4 \Delta v_c^{*k} \end{aligned} \quad (11)$$

where $C_3 = \frac{i_{s0} - 2i_{c0}}{2V_{dc}}$ and $C_4 = \frac{i_{s0} + 2i_{c0}}{2V_{dc}}$.

Equation (11) shows that we need to further find the expressions of the circulating current (i_c^k), the voltage reference related to the circulating current control (v_c^{*k}) and the phase reference voltage (v_s^{*k}). Those expressions should all be related to i_s^k and this will be addressed in the following.

A. Effect of Circulating Current Controller

The circulating current controller is illustrated in Fig. 2. The dynamic equation for the circulating current controller can be expressed by [23]:

$$v_c^{*k}(s) = -R_a [1 + H_c(s)] (i_c^{*k}(s) - i_c^k(s)) - R_c i_c^{*k}(s) \quad (12)$$

With s representing the Laplace variable, i_c^{*k} is the common circulating current reference provided to all three phases and $H_c(s) = \frac{K_r}{R_a} \frac{2s}{s^2 + 2\omega_1^2}$ is the resonant controller to suppress the major second-order harmonic-component in the circulating current. The terms R_a and K_r represent proportional gain of the circulating-current controller and the integral-gain of the resonant controller; whereas, ω_1 is the nominal grid-frequency. The units for the controller gains are given in SI units to conform with the SI units of the various signals. As such, the unit for R_a and K_r are derived from (12) as Ω and Ω^2/sec , respectively. The units for all other controller gains can be expressed similarly in SI units. However, this is skipped in the rest of the paper in order not to hinder readability. Considering that the reference circulating current is zero, the small signal dynamic model of the circulating current controller can be expressed as:

$$\Delta v_c^{*k}(s) = R_a [1 + H_c(s)] \Delta i_c^k(s) \quad (13)$$

Using (13) in (8) and (11), an expression of $\Delta v_{cl}^{\sum k}$ and $\Delta v_{cu}^{\sum k}$ can be obtained in terms of Δi_s^k and Δv_s^{*k} . However, on the assumption that the harmonic content of the circulating current in MMC is dominated by the second harmonic and the amplitude of the other harmonics are much smaller than the second harmonic [25], a simplified expression for the circulating current

in terms of the converter ac current (i_s^k) is given by [25]:

$$\Delta i_c^k(s) \approx \frac{\frac{3m}{8s}}{\underbrace{\frac{4C}{N}(2L_c s + R_c) + \frac{6 + 4m^2}{12s}}_{G_1(s)}} \Delta i_s^k(s) \quad (14)$$

where m is the modulation index. By replacing (14) in (13), the dynamics of the circulating current controller can be expressed in terms of the converter ac current as:

$$\Delta v_c^{*k}(s) = \underbrace{R_a [1 + H_c(s)] G_1(s)}_{G_2(s)} \Delta i_s^k(s) \quad (15)$$

In order to derive the input impedance of the converter, $\Delta v_{cl}^{\sum k}$ and $\Delta v_{cu}^{\sum k}$ in (7) should first be expressed in terms of Δi_s^k and Δv_s^{*k} . This is achieved by substituting (14) and (15) in (11) and using the Laplace transform as:

$$\begin{aligned} \Delta v_{cl}^{\sum k}(s) &= G_3(s) \Delta i_s^k(s) + G_4(s) \Delta v_s^{*k}(s) \\ \Delta v_{cu}^{\sum k}(s) &= G_5(s) \Delta i_s^k(s) + G_6(s) \Delta v_s^{*k}(s) \end{aligned} \quad (16)$$

where $G_3(s) = N [C_1 + 2C_1 G_1(s) - C_3 G_2(s)] / Cs$, $G_4(s) = NC_3 / Cs$, $G_5(s) = N [C_2 + 2C_2 G_1(s) + C_4 G_2(s)] / Cs$, and $G_6(s) = NC_4 / Cs$. Now, by replacing (16) in (7), the ac current dynamics for each phase- k can be expressed in the Laplace domain as:

$$\Delta v_{pcc}^k(s) = G_7(s) \Delta i_s^k(s) + G_8(s) \Delta v_s^{*k}(s) \quad (17)$$

where,

$$\begin{aligned} G_7(s) &= L_t s + R_t + C_1 G_3(s) + C_2 G_5(s) \\ G_8(s) &= 1 + C_1 G_4(s) + C_2 G_6(s) \end{aligned} \quad (18)$$

Now, what is left to find the converter impedance is to find an expression of Δv_s^{*k} in terms of Δi_s^k and Δv_{pcc}^k which will be described in the following sections. However, the derivation of the ac current dynamics in this section has been in a per-phase basis. Assuming that a three-phase balanced system is considered, the expression in (17) can be expressed in the $\alpha\beta$ -frame as:

$$\Delta v_{pcc}^{\alpha\beta}(s) = G_7(s) \Delta i_s^{\alpha\beta}(s) + G_8(s) \Delta v_s^{*\alpha\beta}(s) \quad (19)$$

where the expression in (19) can equivalently be expressed in a rotating dq -frame as

$$\Delta v_{pcc}^{dq}(s) = \underbrace{G_7(s + j\omega_1)}_{G_7^R(s) + jG_7^I(s)} \Delta i_s^{dq}(s) + \underbrace{G_8(s + j\omega_1)}_{G_8^R(s) + jG_8^I(s)} \Delta v_s^{*dq}(s) \quad (20)$$

Using the notation that a bar ($\bar{\cdot}$) indicates a variable in the dq -reference frame represented as a vector using the d - and q -components, (20) can be expressed in component form as:

$$\Delta \bar{v}_{pcc}^c(s) = G_{7,mat}(s) \Delta \bar{i}_s^c(s) + G_{8,mat}(s) \Delta \bar{v}_s^{*c}(s) \quad (21)$$

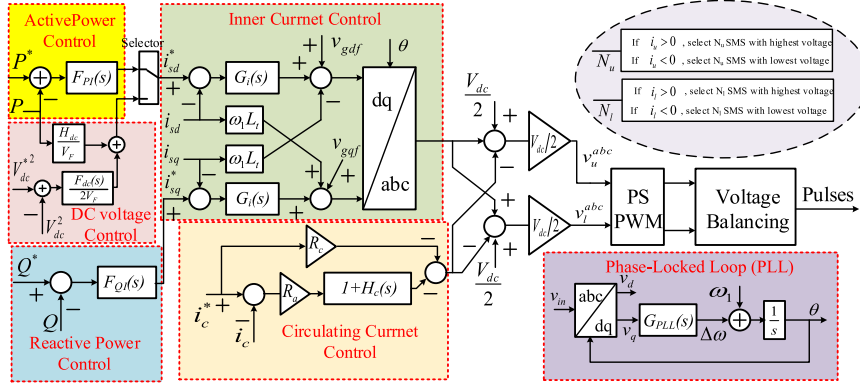


Fig. 2. Vector control of an MMC-HVDC.

where,

$$G_{7,mat}(s) = \begin{bmatrix} G_7^R(s) & -G_7^I(s) \\ G_7^I(s) & G_7^R(s) \end{bmatrix}$$

$$G_{8,mat}(s) = \begin{bmatrix} G_8^R(s) & -G_8^I(s) \\ G_8^I(s) & G_8^R(s) \end{bmatrix} \quad (22)$$

The superscript c denotes that the converter dq -reference frame is used which will be converted to the grid-reference frame using a phase-locked loop (PLL) later.

B. Effect of Inner Current Controller

The next term to be represented in terms of the PCC voltage and the converter current is \bar{v}_s^* , which can be derived from the inner current control loop dynamics in the component form as [26]:

$$v_s^{*dq}(s) = -G_i(s) (i_s^{*dq}(s) - i_s^{dq}(s)) - j\omega_1 L_t i_s^{dq}(s) + \underbrace{\frac{\alpha_f}{s + \alpha_f} v_{pcc}^{dq}(s)}_{H(s)} \quad (23)$$

Note that $G_i(s)$ is a proportional-integral (PI) controller with proportional gain of k_{pi} and integral gain of k_{ii} , and α_f is the bandwidth of a first order low pass filter. For the simplicity in Fig. 2, the dq components of the filtered PCC voltage are shown as v_{gdf} and v_{gqf} .

Applying the small signal analysis to (23) and expressing it in the dq -component form, we have:

$$\Delta \bar{v}_s^{*c}(s) = G_{i,mat}(s) \Delta \bar{i}_s^{*c}(s) + G_{c,mat}(s) \Delta \bar{i}_s^c(s) + H_{mat}(s) \Delta \bar{v}_{pcc}^c(s) \quad (24)$$

where,

$$G_{i,mat}(s) = \begin{bmatrix} -G_i(s) & 0 \\ 0 & -G_i(s) \end{bmatrix}$$

$$G_{c,mat}(s) = \begin{bmatrix} G_i(s) & \omega_1 L_t \\ -\omega_1 L_t & G_i(s) \end{bmatrix}$$

$$H_{mat}(s) = \begin{bmatrix} H(s) & 0 \\ 0 & H(s) \end{bmatrix} \quad (25)$$

As the reference converter current in dq frame (\bar{i}_s^{*c}) is generated by the outer control loops, these will be discussed in the next sections.

C. Effect of Active and Reactive Power Controllers

Outer-loop PI controllers for the active and reactive power controllers are illustrated in Fig. 2, where the d - and q -component of the converter currents control the active and reactive powers, respectively. The power controllers are described as:

$$\begin{cases} i_{sd}^{*c}(s) = (P^* - P)F_{PI}(s) \\ i_{sq}^{*c}(s) = (Q^* - Q)F_{QI}(s) \end{cases} \quad (26)$$

where P^*, Q^* and P, Q are the reference and measured active and reactive powers, respectively. Also, $F_{PI}(s) = k_{pp} + \frac{k_{ip}}{s}$ and $F_{QI}(s) = k_{pq} + \frac{k_{iq}}{s}$ represent the active and reactive power controllers, respectively. Applying the small-signal analysis to (26) leads to:

$$\begin{cases} \Delta i_{sd}^{*c}(s) = -F_{PI}(s) \Delta P \\ \Delta i_{sq}^{*c}(s) = -F_{QI}(s) \Delta Q \end{cases} \quad (27)$$

From the measured active and reactive power as given by $P = v_{pccd}^c i_{sd}^c + v_{pccq}^c i_{sq}^c$, $Q = -v_{pccd}^c i_{sq}^c + v_{pccq}^c i_{sd}^c$ and the steady-state q -component of the PCC voltage is zero ($v_{pccq0} = 0$), we have [26]:

$$\begin{aligned} \Delta P &= i_{sd0} \Delta v_{pccd}^c + i_{sq0} \Delta v_{pccq}^c + v_{pccd0} \Delta i_{sd}^c \\ \Delta Q &= i_{sd0} \Delta v_{pccq}^c - i_{sq0} \Delta v_{pccd}^c - v_{pccd0} \Delta i_{sq}^c \end{aligned} \quad (28)$$

By replacing (28) into (27) and writing it in a matrix form, the reference current is given by

$$\Delta \bar{i}_s^{*c}(s) = \underbrace{\begin{bmatrix} -F_{PI}(s) v_{pccd0} & 0 \\ 0 & F_{QI}(s) v_{pccd0} \end{bmatrix}}_{G_{9,mat}(s)} \Delta \bar{i}_s^c(s) + \underbrace{\begin{bmatrix} -F_{PI}(s) i_{sd0} & -F_{PI}(s) i_{sq0} \\ F_{QI}(s) i_{sq0} & -F_{QI}(s) i_{sd0} \end{bmatrix}}_{G_{10,mat}(s)} \Delta \bar{v}_{pcc}^c(s) \quad (29)$$

D. Effect of DC-Link Voltage Controller

If the outer loop is designed to control the dc-link voltage instead of the active power, the d -component of the reference current will be described as:

$$i_{sd}^{*c}(s) = \frac{F_{dc}(s)(V_{dc}^{*2} - V_{dc}^2)}{2V_F(s)} + \frac{H_{dc}(s)P}{V_F(s)} \quad (30)$$

where $F_{dc}(s) = K_{pdc} + \frac{K_{idc}}{s}$ is a PI regulator for the dc voltage control, and $V_F(s)$ is the measured PCC voltage magnitude passed through a low pass filter, $V_F(s) = H_{dc}(s)|V_{pcc}|$ [26]. The small-signal representation of (30) results in:

$$\Delta i_{sd}^{*c}(s) = -\frac{V_{dc0}F_{dc}(s)}{v_{pccd0}}\Delta V_{dc}(s) - \frac{P_0H_{dc}(s)}{v_{pccd0}^2}\Delta v_{pcc}^c(s) \quad (31)$$

Assuming a loss-less converter, the dc-link dynamics can be described by:

$$\frac{1}{2}C_{dc}\frac{dV_{dc}^2}{dt} = P \Rightarrow C_{dc}V_{dc0}\frac{d\Delta V_{dc}}{dt} = \Delta P \quad (32)$$

where C_{dc} represents the total effective dc-link capacitor of the converter. By substituting (28) in (32), the small-signal model of the dc-link voltage is given by:

$$\begin{aligned} \Delta V_{dc}(s) &= X_1(s)\Delta v_{pcc}^c(s) + X_2(s)\Delta v_{pccq}^c(s) \\ &\quad + X_3(s)\Delta i_{sd}^c(s) \end{aligned} \quad (33)$$

where

$$X_1(s) = \frac{i_{sd0}}{sC_{dc}V_{dc0}}, X_2(s) = \frac{i_{sq0}}{sC_{dc}V_{dc0}}, X_3(s) = \frac{v_{pccd0}}{sC_{dc}V_{dc0}}$$

By replacing (33) in (31), the small-signal representation of the d -component reference current can be derived in terms of the PCC voltage and the ac current as:

$$\begin{aligned} \Delta i_{sd}^{*c}(s) &= X_4(s)\Delta v_{pcc}^c(s) + X_5(s)\Delta v_{pccq}^c(s) \\ &\quad + X_6(s)\Delta i_{sd}^c(s) \end{aligned} \quad (34)$$

where,

$$\begin{aligned} X_4(s) &= -\left(\frac{V_{dc0}F_{dc}(s)X_1(s)}{v_{pccd0}} + \frac{P_0H_{dc}(s)}{v_{pccd0}^2}\right) \\ X_5(s) &= \frac{-V_{dc0}F_{dc}(s)X_2(s)}{v_{pccd0}} \\ X_6(s) &= \frac{-V_{dc0}F_{dc}(s)X_3(s)}{v_{pccd0}} \end{aligned}$$

The derived d -component current reference in (34) can be combined with the q -component in (29) to form $\Delta \tilde{i}_s^{*c}$. Therefore, (29) can be modified in the case of a dc-link voltage

controller to:

$$\begin{aligned} \Delta \tilde{i}_s^{*c}(s) &= \underbrace{\begin{bmatrix} X_6(s) & 0 \\ 0 & F_{QI}(s)v_{pccd0} \end{bmatrix}}_{G_{11,mat}(s)} \Delta \tilde{i}_s^c(s) \\ &\quad + \underbrace{\begin{bmatrix} X_4(s) & X_5(s) \\ F_{QI}(s)i_{sq0} & -F_{QI}(s)i_{sd0} \end{bmatrix}}_{G_{12,mat}(s)} \Delta \bar{v}_{pcc}^c(s) \end{aligned} \quad (35)$$

E. Effect of PLL

Detail analysis of the impact of PLL on the input impedance of a converter has been derived in [26] and the results are adopted here. The main goal is to convert the converter frame variables, $\Delta \tilde{i}_s^c$ and $\Delta \bar{v}_{pcc}^c$, to the grid-reference dq -frame, $\Delta \tilde{i}_s$ and $\Delta \bar{v}_{pcc}$ as:

$$\begin{aligned} \Delta \tilde{i}_s^c(s) &= \Delta \tilde{i}_s(s) - \underbrace{\begin{bmatrix} 0 & \frac{Q_0}{v_{pccd0}}G_{PLL}(s) \\ 0 & \frac{Q_0}{v_{pccd0}}G_{PLL}(s) \end{bmatrix}}_{G_{13,mat}(s)} \Delta \bar{v}_{pcc}(s) \\ \Delta \bar{v}_{pcc}^c(s) &= \underbrace{\begin{bmatrix} 1 & 0 \\ 0 & 1 - v_{pccd0}G_{PLL}(s) \end{bmatrix}}_{G_{14,mat}(s)} \Delta \bar{v}_{pcc}(s) \end{aligned} \quad (36)$$

where $G_{PLL}(s)$ is a simple PI controller given by $G_{PLL}(s) = k_p^{PLL} + \frac{k_i^{PLL}}{s}$. By replacing (36) in (29) or (35), depending on if the active power or the dc-link voltage controller is used, the converter reference current can be described by applying the ac current and the grid voltage in the grid-reference dq -frame. Similarly, the converter voltage reference in (21) and (24) can be expressed in the grid-reference frame using (36).

F. Impedance of MMC

Assuming that the dc-link voltage controller is used instead of the active power controller, the input impedance of the MMC is derived here using (21), (24), (35), and (36). For this, (21) is rewritten using (24) as:

$$\begin{aligned} (I - G_{8,mat}(s)H_{mat}(s))\Delta \bar{v}_{pcc}^c(s) &= (G_{7,mat}(s))\Delta \tilde{i}_s^c(s) \\ &\quad + G_{8,mat}(s)G_{c,mat}(s) + G_{8,mat}(s)G_{i,mat}(s)\Delta \tilde{i}_s^{*c}(s) \end{aligned} \quad (37)$$

where I is an identity matrix. The dynamics in (37) is again rewritten using (35) as

$$G_{15,mat}(s)\Delta \bar{v}_{pcc}^c(s) = G_{16,mat}(s)\Delta \tilde{i}_s^c(s) \quad (38)$$

where,

$$\begin{aligned} G_{15,mat}(s) &= I - G_{8,mat}(s)(H_{mat}(s) - G_{i,mat}(s)G_{12,mat}(s)) \\ G_{16,mat}(s) &= G_{7,mat}(s) + G_{8,mat}(s)(G_{c,mat}(s) \\ &\quad + G_{i,mat}(s)G_{11,mat}(s)) \end{aligned} \quad (39)$$

Finally, the ac current dynamics in the grid-reference dq -frame is expressed by substituting (36) in (38) as:

$$\Delta \bar{v}_{pcc}(s) = Z_{conv}(s)\Delta \tilde{i}_s(s) \quad (40)$$

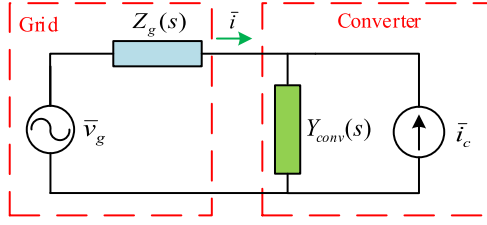


Fig. 3. Impedance model of a converter connected to a grid.

where the input impedance of the converter, $Z_{conv}(s)$ is derived as:

$$Z_{conv}(s) = [G_{15,mat}(s)G_{14,mat}(s) + G_{16,mat}(s)G_{13,mat}(s)]^{-1}G_{16,mat}(s) \quad (41)$$

III. IMPEDANCE STABILITY ANALYSIS

For a grid-connected converter in the current control mode, a Norton equivalent circuit can be developed as in Fig. 3, where $Z_g(s)$ is the grid impedance which can be modeled as:

$$Z_g(s) = \begin{bmatrix} R_g + sL_g & -\omega_1 L_g \\ \omega_1 L_g & R_g + sL_g \end{bmatrix} \quad (42)$$

and \bar{v}_g is the grid voltage at the PCC. Considering $Z_{conv}(s) = Y_{conv}(s)^{-1}$ and according to Fig. 3, the current flowing from the grid to the converter can be derived by:

$$\begin{aligned} \bar{i}(s) &= (\bar{v}_g(s) - Z_{conv}(s)\bar{i}_c(s))[Z_g(s) + Z_{conv}(s)]^{-1} \\ &= (Y_{conv}(s)\bar{v}_g(s) - \bar{i}_c(s))[I + Y_{conv}(s)Z_g(s)]^{-1} \end{aligned} \quad (43)$$

It is assumed that the voltage source ($\bar{v}_g(s)$) is stable when unloaded, i.e. the voltage source has no unstable poles and the load is stable when powered from an ideal voltage source [16]. Therefore, the stability of (43) only depends on the stability of the second term. If the Nyquist plot of $Z_g(s)Y_{conv}(s)$ does not encircle the point $(-1, 0)$, the converter-grid system is stable [16], [20].

IV. CASE STUDIES

In this section, impedance analysis of an MMC connected to a weak grid as in Fig. 1 will be investigated using the Nyquist stability criterion and detailed time-domain simulations will be performed to validate the analytical results for various scenarios. A block-diagram description of the control structure for the proposed system is illustrated in Fig. 2, where the various system and control parameters as well as strategies for the control bandwidth selection can be found in the Appendix. As both the grid and converter impedances are 2×2 matrices, the circuit analysis problem becomes a multi-input multi-output (MIMO) system stability problem. The MIMO system stability criterion is given in [27]. The characteristic function, $\det(I + Y_{conv}(s)Z_g(s)) = 0$ should have no zeros in the right hand plane (RHP). Such stability criterion can be examined by checking the eigen loci of the eigenvalues of $Y_{conv}(s)Z_g(s)$ also known as λ_1, λ_2 [28], [27]. For simplicity, only the dominant eigenvalue (λ_1) is considered and its frequency response, which

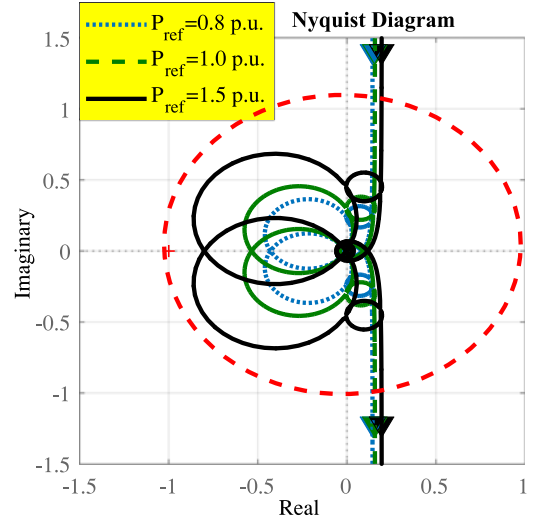


Fig. 4. Analysis results for different MMC power levels. The SCR for this case is set to 1.5.

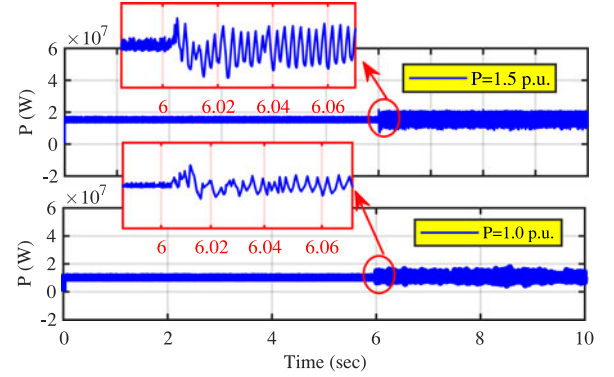


Fig. 5. Simulation results for different MMC power levels. After 6 seconds, the SCR changes from 3 to 1.5.

represents the Nyquist curve of $Y_{conv}(s)Z_g(s)$ is plotted for each case.

A. Impact of Different MMC Power Levels

If both V_g and V_{pcc} are 1.0 p.u. in normal operation, the maximum theoretical power transfer is $SCR \sin(\theta_g - \theta_v)$ [14]. The load angle cannot be beyond 90 degrees, therefore, the maximum power transfer is approximately equal to the short-circuit ratio (SCR) of the system ($P_{max} \approx SCR$). Hence, the SCR poses theoretical limitation on power transfer. In this case, the effect of different MMC power levels will be investigated. The SCR of the system is considered as 1.5 and power levels change from 0.8 p.u. to 1.5 p.u. Nyquist stability analysis results are shown in Fig. 4. It is observed that the system is stable for all three power transfer levels, however, the stability is decreased by increasing the power transfer as Nyquist plots get closer to the point $(-1, 0)$. In this case, $P_{max} \approx SCR = 1.5$ p.u., therefore, the system cannot transfer more than 1.5 p.u.

For the time-domain simulations as shown in Fig. 5, two power-transfer levels are considered. With the base power being set to 10 MW, the SCR of the system is changed from 3 (strong

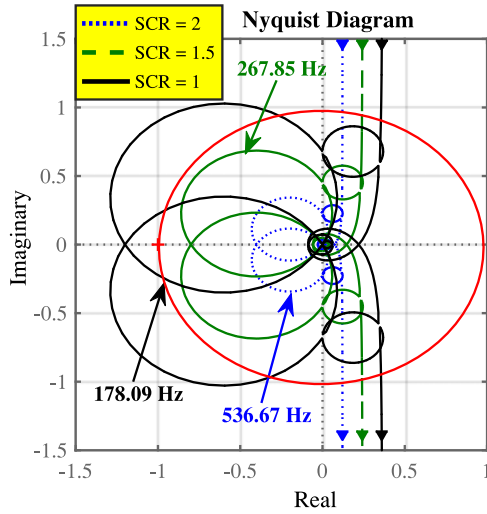


Fig. 6. Analysis results for different SCRs values.

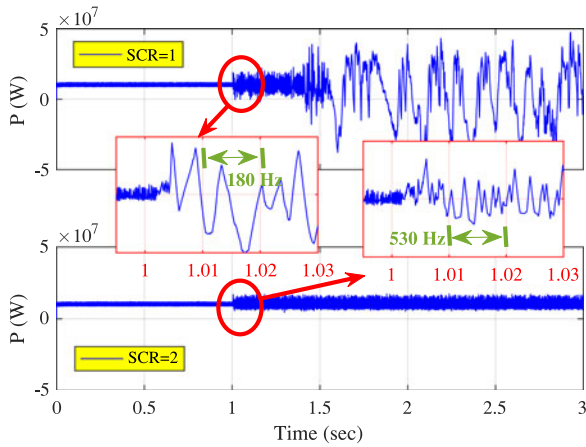


Fig. 7. Simulation results for different SCR values.

system) to 1.5 (weak system) after 6 seconds. It is observed that the system is stable for both power transfer levels. The simulation results appear to be in agreement with the analytical results shown in Fig. 4 confirming the validity of the analysis.

B. Impact of Different SCR Values

This case is designed to investigate the interactions between the MMC controller and the grid when the grid strength changes. Three different SCRs have been considered in this case. Nyquist plots for various SCR values are illustrated in Fig. 6. It is demonstrated that the system is stable when the SCR values are 2 and 1.5. However, when the system is weaker with $SCR = 1$, the Nyquist plot encircles the point $(-1, 0)$, which results in an unstable resonance of around 180 Hz between the MMC and the grid. The resonance frequency is found to be 267 Hz for the case of $SCR = 1.5$ and 536 Hz for $SCR = 2$. For the time-domain simulations, the SCR of the system is modified from 2 to 1 in order to test the interactions between the MMC and the grid in weak ac grid connections. The converter is initially operating at 10 MW with $SCR = 3$ and the SCR will be changed at 1 second. Simulation results are shown in Fig. 7. It is observed that the system is stable when $SCR = 3$ before 1 second. However, after

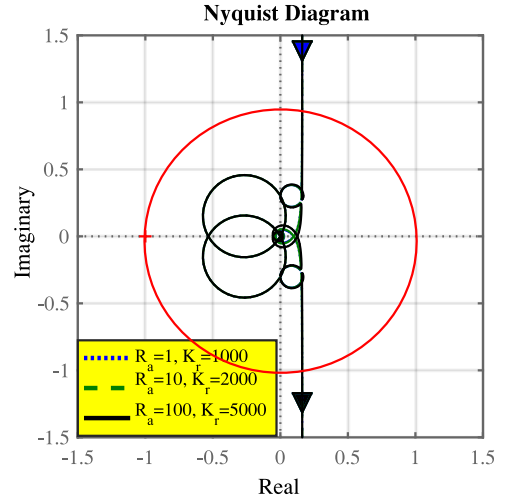


Fig. 8. Analysis results for different PR controller gains when the converter is controlling the active and reactive power.

changing the SCR to 2, a 530 Hz oscillation is observed. By changing the SCR from 3 to 1 at 1 second, 180 Hz resonance will be observed in the beginning which finally causes instability to the system and the MMC is not able to transfer the power in this condition. Simulation results are also in agreement with Fig. 6, where the Nyquist plot encircled the point $(-1, 0)$ when $SCR = 1$. Similarly, for $SCR = 2$, the Nyquist plot in Fig. 6 did not encircle the point $(-1, 0)$.

C. Impact of PR Controller Gains With Active Power Control

In this scenario, the effect of the PR controller on the system stability is studied when the MMC is enhanced with an active and reactive power controller. The Nyquist plots for multiple PR controller gains are shown in Fig. 8. The SCR of the system is set to 1.5. It appears that the PR controller does not have much impact on the stability of the system when the converter is controlling the active and reactive powers. This is in agreement with [29] that the PR controller with large gains has lower risks of harmonic instability when the converter is controlling the active power (instead of controlling the dc voltage). This shows that the Nyquist plots will not change significantly by changing the PR controller gains.

Simulation results are shown in Fig. 9, where the SCR value of the system is changed from 3 to 1.5 after 5 seconds and the power transfer level is set to 10 MW. It can be observed that changing the PR controller parameters has no significant impact on the system stability. The results are in agreement with Fig. 8, where the Nyquist plots are the same for the different PR gains. However, it is evident from the circulating current results on the right hand side of Fig. 9 that increasing the PR controller gains improves the PR controller performance. Therefore, if an MMC is controlling the active and reactive powers, high PR controller gains provide a better response.

D. Impact of PR controller Gains With DC Voltage Control

It was stated in [29] that when the converter is controlling the dc voltage, the sensitivity of the PR controller parameters is higher. Nyquist plots for the MMC operating at $SCR = 1.5$

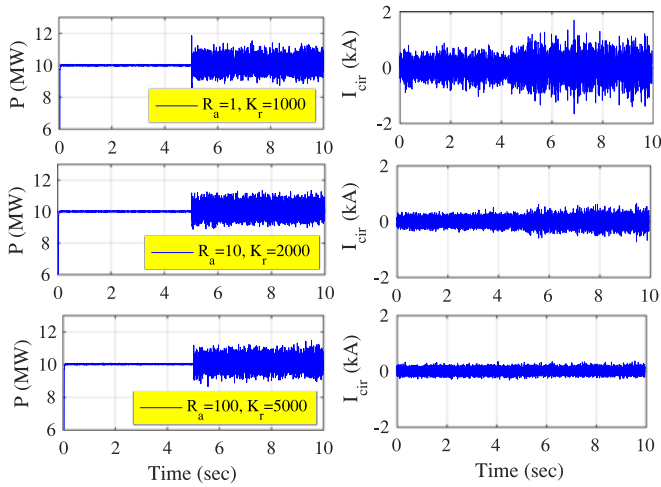


Fig. 9. Simulation results for the PR gain change effect on the active power controller of the MMC system. The SCR changes from 3 to 1.5 after 5 seconds.

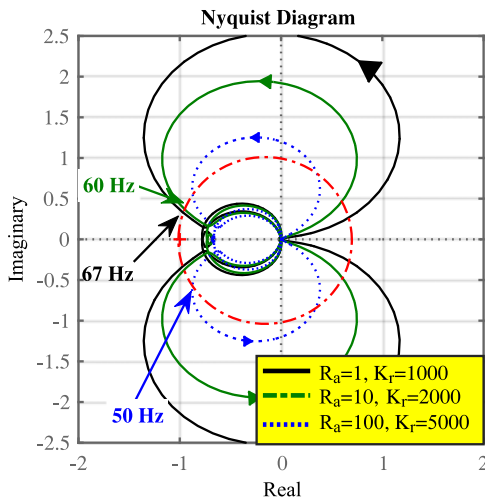


Fig. 10. Analysis results for different PR controller gains when the MMC is enhanced with the dc voltage and reactive power control.

enhanced with the dc voltage and reactive power controller are illustrated in Fig. 10. The results suggest that increasing the PR controller gains will decrease the resonance frequency of the interactions between the converter and the grid. The resonant frequency of the oscillations for $K_p = 1$, $K_r = 1000$ is 70 Hz which will decrease up to 50 Hz for $K_p = 100$, $K_r = 5000$.

The simulation results for the different PR controller gains when the MMC is enhanced with the dc voltage controller are illustrated in Fig. 11. It is clear that the PR controller has a significant impact on the dc voltage control loop. Increasing the PR controller will deteriorate the performance of the dc voltage control. The simulation results agree with the impedance analysis results shown in Fig. 10, which proves the validity of the analysis results. It is also concluded from the circulating current results, shown in the right hand side of Fig. 11, that increasing the PR controller gains in case the MMC is controlling the dc voltage will deteriorate the performance of the PR controller and the dc voltage controller. Hence, the PR controller gains should be smaller in this case.

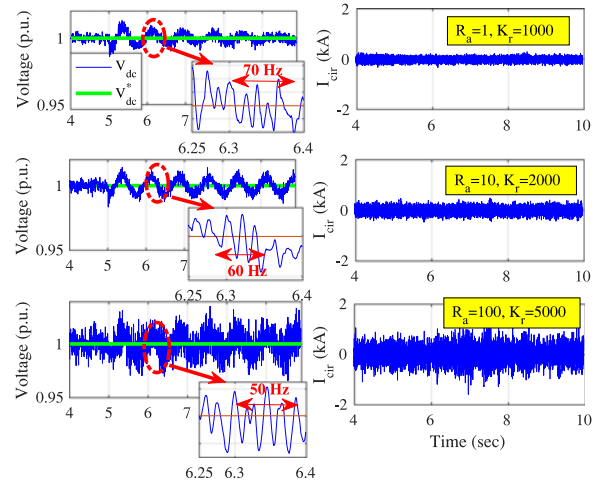


Fig. 11. Simulation results for the effect of PR gain change on the dc voltage controller of the MMC system. The SCR changes from 3 to 1.5 after 5 seconds.

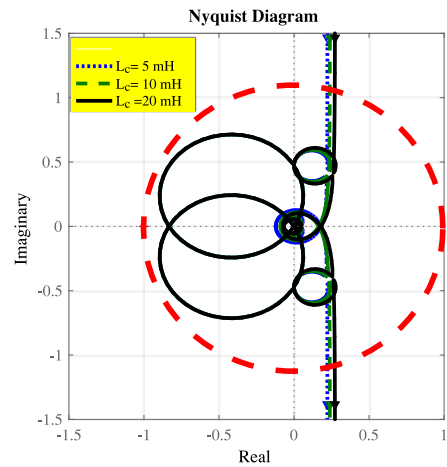


Fig. 12. Analysis results for different arm inductances when the MMC is enhanced with the active and reactive power control.

E. Impact of Arm Inductance

In this section, the effect of different arm inductance values on the stability of the MMC-HVDC system connected to a weak ac grid is investigated. The arm inductance is normally selected between 0.1 p.u. to 0.3 p.u., but low values are suitable for stability analysis. In this section, three different values ($L_c = 20$ mH (≈ 0.2 p.u.), $L_c = 10$ mH (≈ 0.1 p.u.) and $L_c = 5$ mH (≈ 0.05 p.u.) are selected. The Nyquist plots for the MMC operating at SCR = 1.5 enhanced with the active and reactive power controllers are illustrated in Fig. 12. The arm inductance is decreased to evaluate the effect on the system stability. As it can be seen, decreasing the arm inductance does not cause encirclement of the point $(-1, 0)$ and the system remains stable.

Time-domain simulation results for the same case study are shown in Fig. 13. The system is operating at steady state with SCR = 3 when the SCR is changed to 1.5 after 5 seconds. As shown in Fig. 13, decreasing the arm inductance does not have much impact on the active power waveform, except high frequency ripples (400 Hz) occur when the SCR changes to 1.5. Although the system is stable in this case, the circulating current controller performance will be deteriorated as the arm

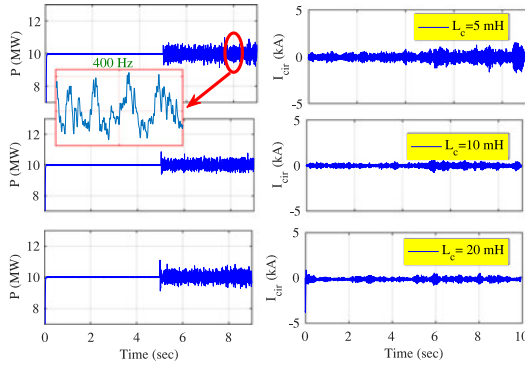


Fig. 13. Simulation results for different arm inductance values. After 5 seconds, the SCR changes from 3 to 1.5.

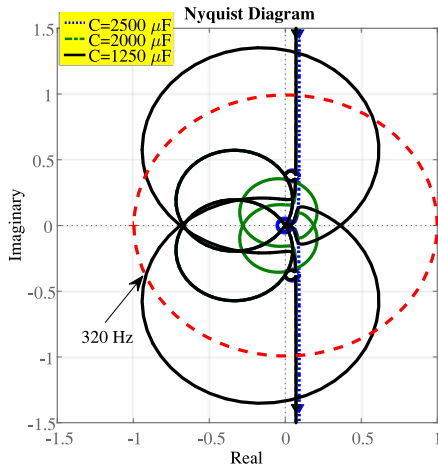


Fig. 14. Analysis results for different submodule capacitances when the MMC is enhanced with the active and reactive power control.

inductance decreases. Therefore, lower arm inductance values cause stability issues for circulating current controller.

F. Impact of SM Capacitance

The effect of SM capacitance on the stability of the MMC in a weak ac grid connection is studied in this case. The SM capacitance should be selected in away to make the SM voltage ripple within 10% of the nominal voltage. For the analysis, the SM capacitance is decreased and the Nyquist plots are shown in Fig. 14. It can be understood that decreasing the capacitance value from 2500 μF to 1250 μF in weak ac grids causes 320 Hz resonances. Even though none of the Nyquist plots encircle the point $(-1, 0)$ indicating that the system remains stable, the stability margin of the system is drastically reduced as indicated in the Nyquist plots in Fig. 14 and the time-domain simulation in Fig. 15.

In the time-domain simulation illustrated for the same case study, the system is initially operating at $\text{SCR} = 3$ until it is changed to 1.5 after 5 seconds. As the results show, decreasing the SM capacitance causes 320 Hz oscillations in active power waveform as showed earlier in Nyquist plots, too. Decreasing the SM capacitance also deteriorates the performance of the circulating current controller as shown in the right hand side plots in Fig. 15.

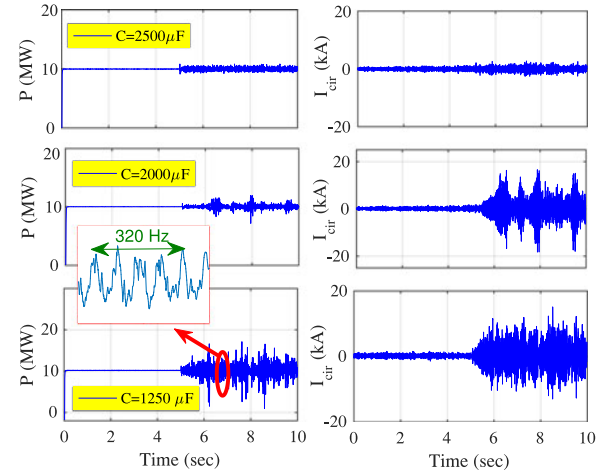


Fig. 15. Simulation results for different submodule capacitance values. After 5 seconds, the SCR changes from 3 to 1.5.

V. CONCLUSION

This paper deals with the impedance analysis of an MMC connected to a weak ac grid. The converter impedance including various control structures is derived. The Nyquist-stability criterion is then used to analyze the interactions between the MMC and the grid. Multiple case studies are defined for which time-domain simulations are carried out to validate the analytical results. It is concluded that the MMC performance in power transfer is limited when the system is weak. The results show that increasing the power transfer level in weak ac grids reduces the stability margin of the system. Moreover, the analysis results demonstrate that the weakness of the ac grid also affects the stability margins; the smaller the SCR value, the less stable the system. Furthermore, the proportional-resonant (PR)-based circulating current controller has a negligible impact on the stability of the system when the MMC is enhanced with an active and reactive power controllers. On the other hand, the PR-controller gains have a significant impact on the stability of the system when the MMC is controlling the dc voltage. It has also been shown that the arm inductance has minimum impact on the stability of the system if it is selected between 0.1 to 0.3 p.u. The analysis also indicated that low SM capacitance values cause resonances in weak ac grid connections. Therefore, the SM capacitance should be selected in such a way that the voltage ripple in the SM capacitor is within 10% of the nominal voltage.

ACKNOWLEDGMENT

The authors would like to especially acknowledge Dr. Lingling Fan for her continuous support and Dr. Lakshan Piyasinghe for his helpful feedback on this work.

APPENDIX

A. Table of Parameters

The various system and control parameters for the study are given in Tables I and II.

TABLE I
SYSTEM PARAMETERS OF MMC MODEL [22]

Quantity	Value
Base voltage	20 kV
Base frequency	60 Hz
Base power	10 MW
DC rated voltage	60 kV
Submodules per arm	4
Grid inductance	0.1 H for SCR = 1, 0.035 H for SCR = 3
R_c, L_c	0.1 Ω , 0.02 H
R_f, L_f	0.2 Ω , 0.02 H
C	2500 μF
ω_1	377 rad/sec

TABLE II
PARAMETERS OF CONTROLLERS [22]

Quantity	Value
Power controller ($F_{PI}(s)$)	$k_{pp} = 40, k_{pi} = 1000$
DC voltage controller ($F_{DC}(s)$)	$k_{pdc} = 5, k_{idc} = 100$
Reactive power controller ($F_{QI}(s)$)	$k_{pq} = 40, k_{iq} = 1000$
Inner current control ($G_i(s)$)	$k_{pi} = 30, k_{ii} = 250$
PR controller	$k_r = 1000, R_a = 1$
PLL ($G_{PLL}(s)$)	$k_p^{PLL} = 180, k_f^{PLL} = 3200$
Bandwidth of $H(s)$	$\alpha_f = 100 \pi$ rad/s
Bandwidth of $H_{dc}(s)$	$\alpha_{dc} = 60 \pi$ rad/s

B. Parameter Selection for Controllers

The conventional bandwidth decoupling approach is used to select the parameters of the PI controllers for each loop. Detailed information about the bandwidth decoupling approach can be found in [3], but the bandwidth design for the inner current controller and the outer power controller are included here and the parameters for the other loops can be selected accordingly. To achieve this goal, the inner current-control loop was first designed to track the reference currents with minimum overshoot and settling time. The outer control loops were then designed to be slower than the inner loop but with minimum overshoot and settling time. The initial parameters were selected based on [22].

1) *Inner-Current Control Loop*: The inner current control loop should be designed much faster than the outer loops. The converter voltage and current in abc frame are represented as v_{abc} and i_{abc} . Considering the voltage at the PCC as v_{PCC} and assuming that the converter's d -axis is aligned with the PCC voltage's space vector, the dynamics of the ac grid can be represented as:

$$L_f \frac{d(i_d + ji_q)}{dt} + (R_f + j\omega L_f)(i_d + ji_q) = v_d + jv_q - v_{sd} \quad (44)$$

where $v_d + jv_q$ is the PCC voltage converted to the dq reference frame, and $i_d + ji_q$ is the dq reference frame current flowing from the PCC to the converter. By separating the real

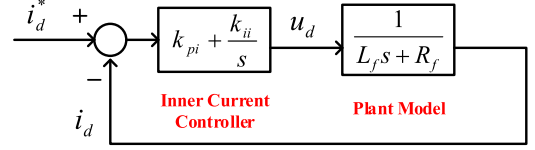


Fig. 16. Simplified representation of inner-current loop.

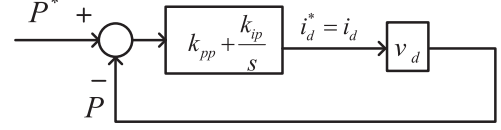


Fig. 17. simplified representation of outer-loop power controller.

and imaginary components of (44) and rearranging:

$$\begin{aligned} L_f \frac{di_d}{dt} + R_f i_d &= \underbrace{v_d - v_{sd} + \omega L_f i_q}_{u_d} \\ L_f \frac{di_q}{dt} + R_f i_q &= \underbrace{v_q - \omega L_f i_d}_{u_q} \end{aligned} \quad (45)$$

Therefore, the plant model for the inner current controller is $\frac{1}{R_f + sL_f}$ for both dq -axes. The inputs are u_d and u_q while the outputs are i_d and i_q . Feedback controls are designed for the dq -axis currents to track the reference currents. Furthermore, the designed control outputs should add the cross coupling terms to generate dq components of the converter voltage. A simplified structure of the inner current controller with plant model is considered in Fig. 16. The loop gain for the system is expressed as:

$$l(s) = \frac{k_{pi}}{L_f s} \left(\frac{s + \frac{k_{ii}}{k_{pi}}}{s + \frac{R_f}{L_f}} \right) \quad (46)$$

It was mentioned in [3] that the plant pole is fairly close to the origin. Therefore, the plant pole is canceled by the compensator zero and the loop gain becomes $\frac{k_{ip}}{L_f s}$. As a result, the closed loop transfer function of the inner current controller for the d axis can be represented as:

$$G_{inner}(s) = \frac{l(s)}{1 + l(s)} = \frac{1}{\tau_{in} s + 1} \quad (47)$$

where $\tau_{in} = \frac{L_f}{k_{pi}}$ and $k_{ii} = \frac{R_f}{\tau_{in}}$ and the bandwidth of the controller is defined as $\omega_{inner} = \frac{1}{\tau_{in}}$. The inner loop gains are designed so that the bandwidth of the inner loop with $k_{pi} = 30$ and $k_{ii} = 250$ and the ac filter ($L_f = 0.03$ H) is around 1000 rad/s.

2) *Outer-Control Loops*: When the outer loops are designed, the inner loop is considered to be very fast so that the current orders can be followed immediately, i.e. $i_d^* = i_d$ and $i_q^* = i_q$. The simplified block diagram of the outer control loop for the active power is illustrated in Fig. 17. A similar analysis can be carried out for the dc voltage and reactive-power control loops, which are skipped in this section and more information can be found in [3].

As the dq reference frame is aligned with the PCC voltage, the real and reactive powers can be represented as $P = v_d i_d$ and

$Q = v_d i_q$. Therefore, a closed-loop simplified transfer function for the outer power loop is expressed as:

$$G_{outp} = \frac{\left(k_{pp} + \frac{k_{ip}}{s}\right) v_d}{1 + \left(k_{pp} + \frac{k_{ip}}{s}\right) v_d} = \frac{\frac{k_{pp}}{k_{ip}} s + 1}{\left(\frac{1}{v_d k_{ip}} + \frac{k_{pp}}{k_{ip}}\right) s + 1} \quad (48)$$

This is a first order transfer function to the form of $\frac{as+1}{\tau s+1}$, where τ is the time constant ($\tau = \frac{1}{v_d k_{ip}} + \frac{k_{pp}}{k_{ip}}$) and the outer power loop bandwidth can be found as $\frac{1}{\tau}$. In this study, the outer power loop gains are designed so that the bandwidth of the outer loop with $k_{pp} = 40$ and $k_{ip} = 1000$ is around 25 rad/s which is much lower than the inner current controller bandwidth. With the same analysis, the bandwidth of the reactive power controller is designed to be around 25 rad/s and the bandwidth of the dc voltage controller is around 20 rad/s.

REFERENCES

- [1] M. Saeedifard and R. Iravani, "Dynamic performance of a modular multilevel back-to-back HVDC system," *IEEE Trans. Power Del.*, vol. 25, no. 4, pp. 2903–2912, Oct. 2010.
- [2] R. Marquardt, "Modular multilevel converter: A universal concept for HVDC-networks and extended dc-bus-applications," in *Proc. IEEE 2010 Int. Power Electron. Conf.*, 2010, pp. 502–507.
- [3] A. Yazdani and R. Iravani, *Voltage-Sourced Converters in Power Systems: Modeling, Control, and Applications*. Hoboken, NJ, USA: Wiley, 2010.
- [4] N. Flourentzou, V. G. Agelidis, and G. D. Demetriades, "VSC-based HVDC power transmission systems: An overview," *IEEE Trans. Power Electron.*, vol. 24, no. 3, pp. 592–602, Mar. 2009.
- [5] Q. Tu, Z. Xu, and L. Xu, "Reduced switching-frequency modulation and circulating current suppression for modular multilevel converters," *IEEE Trans. Power Del.*, vol. 26, no. 3, pp. 2009–2017, Jul. 2011.
- [6] J. Moon, C. Kim, J. Park, D. Kang, and J. Kim, "Circulating current control in MMC under the unbalanced voltage," *IEEE Trans. Power Del.*, vol. 28, no. 3, pp. 1952–1959, Jul. 2013.
- [7] Q. Tu, Z. Xu, and J. Zhang, "Circulating current suppressing controller in modular multilevel converter," in *Proc. IECON 2010 36th Annu. Conf. IEEE Ind. Electron. Soc.*, 2010, pp. 3198–3202.
- [8] Q. Song, W. Liu, X. Li, H. Rao, S. Xu, and L. Li, "A steady-state analysis method for a modular multilevel converter," *IEEE Trans. Power Electron.*, vol. 28, no. 8, pp. 3702–3713, Aug. 2013.
- [9] M. Mehra, E. Pouresmaeil, S. Zabihi, and J. P. Catalao, "Dynamic model, control and stability analysis of MMC in HVDC transmission systems," *IEEE Trans. Power Del.*, vol. 32, no. 3, pp. 1471–1482, Jun. 2017.
- [10] G. Tang, Z. Xu, and Y. Zhou, "Impacts of three MMC-HVDC configurations on ac system stability under dc line faults," *IEEE Trans. Power Syst.*, vol. 29, no. 6, pp. 3030–3040, Nov. 2014.
- [11] J. Lyu, X. Cai, and M. Molinas, "Frequency domain stability analysis of MMC-based HVDC for wind farm integration," *IEEE J. Emerg. Sel. Topics Power Electron.*, vol. 4, no. 1, pp. 141–151, Mar. 2016.
- [12] A. Egea-Alvarez, S. Fekriasl, F. Hassan, and O. Gomis-Bellmunt, "Advanced vector control for voltage source converters connected to weak grids," *IEEE Trans. Power Syst.*, vol. 30, no. 6, pp. 3072–3081, Nov. 2015.
- [13] M. Davari and Y. A. R. I. Mohamed, "Robust vector control of a very weak-grid-connected voltage-source converter considering the phase-locked loop dynamics," *IEEE Trans. Power Electron.*, vol. 32, no. 2, pp. 977–994, Feb. 2017.
- [14] L. Zhang, L. Harnefors, and H. P. Nee, "Interconnection of two very weak ac systems by VSC-HVDC links using power-synchronization control," *IEEE Trans. Power Syst.*, vol. 26, no. 1, pp. 344–355, Feb. 2011.
- [15] C. Guo, W. Liu, C. Zhao, and R. Iravani, "A frequency-based synchronization approach for the VSC-HVDC station connected to a weak ac grid," *IEEE Trans. Power Del.*, vol. 32, no. 3, pp. 1460–1470, Jun. 2017.
- [16] J. Sun, "Impedance-based stability criterion for grid-connected inverters," *IEEE Trans. Power Electron.*, vol. 26, no. 11, pp. 3075–3078, Nov. 2011.
- [17] B. Wen, D. Dong, D. Boroyevich, R. Burgos, P. Mattavelli, and Z. Shen, "Impedance-based analysis of grid-synchronization stability for three-phase paralleled converters," *IEEE Trans. Power Electron.*, vol. 31, no. 1, pp. 26–38, Jan. 2016.
- [18] M. Amin and M. Molinas, "Understanding the origin of oscillatory phenomena observed between wind farms and HVDC systems," *IEEE J. Emerg. Sel. Topics Power Electron.*, vol. 5, no. 1, pp. 378–392, Mar. 2017.
- [19] L. Xu, L. Fan, and Z. Miao, "DC impedance-model-based resonance analysis of a VSC-HVDC system," *IEEE Trans. Power Del.*, vol. 30, no. 3, pp. 1221–1230, Jun. 2015.
- [20] L. Xu and L. Fan, "Impedance-based resonance analysis in a VSC-HVDC system," *IEEE Trans. Power Del.*, vol. 28, no. 4, pp. 2209–2216, Oct. 2013.
- [21] J. Lyu, X. Cai, and M. Molinas, "Impedance modeling of modular multilevel converters," in *Proc. IECON 2015-41st Annu. Conf. IEEE Ind. Electron. Soc.*, Nov. 2015, pp. 000180–000185.
- [22] Y. Ma and L. Fan, "Circulating current and dc current ripple control in MMC under unbalanced grid voltage," in *Proc. 2015 North Amer. Power Symp.*, Oct. 2015, pp. 1–6.
- [23] L. Harnefors, A. Antonopoulos, S. Norrga, L. Angquist, and H.-P. Nee, "Dynamic analysis of modular multilevel converters," *IEEE Trans. Ind. Electron.*, vol. 60, no. 7, pp. 2526–2537, Jul. 2013.
- [24] M. Beza, M. Bongiorno, and G. Stamatiou, "Analytical derivation of the ac-side input admittance of a modular multilevel converter with open- and closed-loop control strategies," *IEEE Trans. Power Del.*, to be published.
- [25] K. Ilves, A. Antonopoulos, S. Norrga, and H. P. Nee, "Steady-state analysis of interaction between harmonic components of arm and line quantities of modular multilevel converters," *IEEE Trans. Power Electron.*, vol. 27, no. 1, pp. 57–68, Jan. 2012.
- [26] L. Harnefors, M. Bongiorno, and S. Lundberg, "Input-admittance calculation and shaping for controlled voltage-source converters," *IEEE Trans. Ind. Electron.*, vol. 54, no. 6, pp. 3323–3334, Dec. 2007.
- [27] M. C spedes and J. Sun, "Modeling and mitigation of harmonic resonance between wind turbines and the grid," in *Proc. 2011 IEEE Energy Convers. Congr. Expo.*, Sep. 2011, pp. 2109–2116.
- [28] L. Piyasinghe, Z. Miao, J. Khazaei, and L. Fan, "Impedance model-based SSR analysis for TCSC compensated type-3 wind energy delivery systems," *IEEE Trans. Sustain. Energy*, vol. 6, no. 1, pp. 179–187, Jan. 2015.
- [29] T. Li, A. Gole, and C. Zhao, "Stability of a modular multilevel converter based HVDC system considering dc side connection," in *Proc. 12th IET Int. Conf. AC DC Power Transmiss.*, May 2016, pp. 1–6.



Javad Khazaei (S'10–M'16) received the Ph.D. degree from the University of South Florida (USF), Tampa, FL, USA, in 2016. He is currently an Assistant Professor with the School of Science, Engineering and Technology, Penn State Harrisburg, Middletown, PA, USA. His research interests include micro-grid modeling, dynamic analysis of power converters in smart grids, application of distributed optimization in smart grids, renewable energy integration, and power electronics applications in power systems.



Mebtu Beza (S'13–M'15) received the M.Sc., Lic.Eng., and Ph.D. degrees in electric power engineering from Chalmers University of Technology, Gothenburg, Sweden, in June 2009, June 2012, and February 2015, respectively. He is currently a Post-doctoral Researcher with Chalmers University of Technology. His research interests include signal processing in power systems, control theory, stability studies in VSC-HVDC systems, and application of power electronics in power systems.



Massimo Bongiorno (S'02–M'07–SM'16) received the M.Sc. degree in electrical engineering from the University of Palermo, Palermo, Italy, in April 2002, and the Lic.Eng. and Ph.D. degrees from Chalmers University of Technology, Gothenburg, Sweden, in December 2004 and September 2007, respectively. From 2007 to 2010, he was an Assistant Professor with the Department of Electric Power Engineering, Chalmers University of Technology, where he became an Associate Professor in 2010. Since 2015, he has been holding the position of a Professor in power electronic applications for power systems. His research interests include application of power electronics in power systems, power system dynamics, and power quality.